Understanding Power Transformer Frequency Response Analysis Signatures

A. Abu-Siada, N. Hashemnia, S. Islam, and Mohammad A.S. Masoum
Electrical and Computer Engineering Department, Curtin University, Western Australia

SUMMARY
Data obtained using a distributed parameter model to simulate a power transformer are presented. These data could be used in the formulation of standard codes for interpretation of the frequency response analysis signatures of power transformers.

Key Words: Power transformer, FRA, condition monitoring, winding deformation.

I. INTRODUCTION

THE majority of transformers currently in service worldwide were installed prior to 1980, and consequently most of them are approaching or have already exceeded their design lifetimes [1, 2]. This poses a significant risk for utilities and other power network stakeholders, since the impact of in-service transformer failure can be catastrophic. One of the most serious problems with an in-service transformer is movement of its windings due to electromagnetic forces generated during short circuit faults. Reduction of clamping pressure due to insulation aging can also cause winding movement, and may result in an explosion [3-6]. There are many causes of mechanical faults, e.g., earthquake, explosion of combustible gas in the transformer oil, short circuit currents, and careless transportation [7,8]. While a transformer with minor winding deformation may continue to work satisfactorily, its capability to withstand further mechanical or electrical faults will gradually decrease [9]. Therefore it is essential to detect any minor winding deformation as soon as possible, and to take appropriate remedial action. Winding deformation has various forms, e.g., spiral tightening, conductor tilting, radial/hoop buckling, shorted or open turns, loosened clamping structures, axial displacement, core movement, and collapse of the winding end supports. It is difficult to differentiate between these internal faults using conventional testing methods [10].

In this article data obtained using a high frequency distributed parameter model to simulate a power transformer are presented. Mechanical faults such as axial displacement, radial buckling, disk space variation, loss of clamping, bushing and leakage faults were simulated by modifying the relevant electrical parameters in the transformer model, or by reconfiguring the impacted disks in a 3D transformer finite element model. It is suggested that the resulting data could be used in the formulation of standard codes for interpretation of the frequency response analysis signatures of power transformers.

II. FREQUENCY RESPONSE ANALYSIS

Frequency response analysis (FRA) is a powerful diagnostic technique widely used to identify internal faults within power transformers [11]. Transformer components such as windings, core and insulation can be represented by equivalent circuits comprising resistors, capacitors, and self / mutual inductances, whose values will be altered by a mechanical fault within the transformer. Thus the frequency response of the relevant equivalent circuit winding will change. Changes in ttransformer geometry, or in the dielectric properties of insulating materials due to ageing or increasing water content, also affect the shape of the frequency response, especially the resonant frequencies and their damping [8].

FRA is an offline technique in which a low voltage ac signal is injected at one terminal of a winding, and the response is measured at the other terminal of the same winding with reference to the grounded tank. The FRA analyzer measures the transfer function, impedance or admittance of the winding, typically over the frequency range 10 Hz - 2 MHz, and one or all of these three properties can be used for fault diagnosis. Although the FRA equipment can be connected to the transformer in different ways [12-14], end-to-end connection shown in Fig. 1 is capable of detecting the main types of mechanical faults [14].

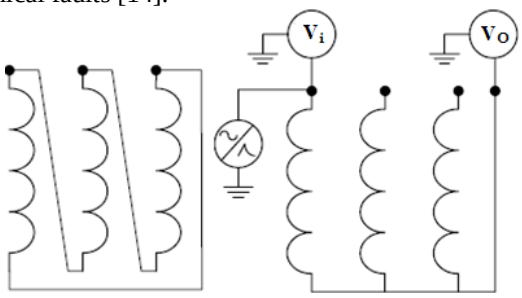

Fig. 1. FRA end-to-end test configuration

The FRA signature is considered as a fingerprint of the transformer, which can be compared with a previous signature in order to detect any mechanical deformation which may have developed between the recording of the two signatures. FRA diagnosis has also been utilized recently to identify winding deformations in rotating machines [13]. While the measurement procedure using commercial test equipment is quite simple, skilled and experienced personnel are required in order to interpret the FRA signatures and identify correctly the type and location of a fault. Although much research has been done on this topic, a reliable FRA signature interpretation code has not yet been published.

The authors of [14] sub-divide the FRA frequency range as follows:

(a) the low frequency range (<20 kHz), within which inductive components dominate the transformer winding response

(b) the medium frequency range (20–400 kHz), within which the combination of inductive and capacitive components results in multiple resonances

(c) the high frequency range (>400 kHz), within which capacitive components dominate the FRA signature [15]. These ranges and the associated fault types are summarized in Table I [16, 17].

TABLE I
FRA BANDS AND THEIR SENISTIVITY TO FAULTS [16]

Frequency Band	Fault sensitivity
< 20kHz	Core deformation, open circuits, shorted turns and residual magnetism, bulk winding movement, clamping structure loosening
20 - 400 kHz	Deformation within the main or tap windings
> 400 kHz	Movement of the main and tap windings, ground impedances variations

III. Transformer Model and Sensitivity Analysis

Simplorer software was used to simulate the transformer model shown in Fig. 2 [17-19].

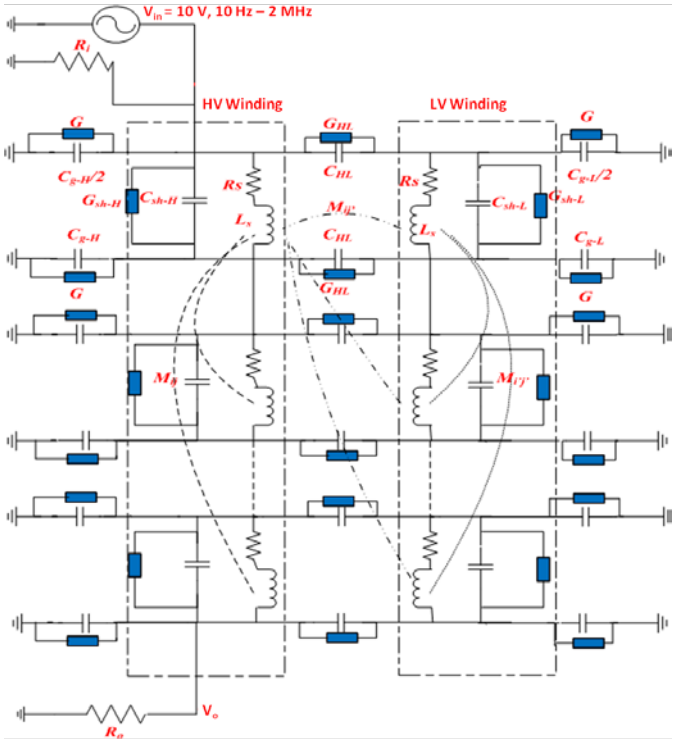

Fig. 2. 10-disk model of a transformer [17].

The high voltage (HV) and low voltage (LV) windings are each assumed to consist of 10 disks. Each disk comprises a series resistance (R_s) and inductance (L_s), shunted by a capacitor (C_{sh}) and a conductance (G_{sh}). The capacitance (C_{HL}) between the HV and LV windings is shunted by a dielectric conductance (G_{HL}), and mutual inductances (M_{ij}) between coils i and j are included. The dielectric insulation (oil) between the LV winding and the core, and between the HV winding and the tank, is simulated by a capacitance (C_g) and dielectric conductance (G). The fault-free component values of the model given in [9] and [13] are listed in the Appendix.

In Table II the transformer model parameters, and the mechanical faults which influence them, are listed. Various mechanical faults can be simulated by changing relevant parameters in the transformer model. This can aid in establishing a standard code for FRA signature interpretation.

Table II
MODEL PARAMETERS AND THE MECHANICAL FAULTS WHICH INFLUENCE THEM [9], [11], [17], [20]-[23]

Model Parameter	Type of Fault
Inductance L_s	Disk deformation, local breakdown, core deformation and winding short circuits.
Shunt Capacitance C_{sh}	Disk movements, buckling due to large mechanical forces, moisture ingress and loss of clamping pressure.
Series Capacitance C_{HL}	Ageing of insulation, moisture ingress and disk movement.
Resistance R_s	Shorted or broken disk, failure of caulking contacts and tap changer contact wear.

The sensitivity of the FRA signature to variation of the model parameters was investigated. As shown in Fig. 2, a sinusoidal excitation voltage (V_{in}) of 10 V and variable frequency (10 Hz to 2 MHz) is connected to one winding terminal, and the response at the other terminal of the winding (V_o) is recorded. The input/output coaxial leads used in practical measurements are represented by 50Ω resistors (R_i and R_o in Fig. 2). The transfer function $TF_{dB} = 20 \log_{10} |V_0/V_{in}|$ is plotted against frequency. Fig. 3 shows the effect of ±10% changes in the capacitances C_g and C_{sh} of the HV winding on the FRA signature, compared to the base line (fingerprint) signature. Increasing C_{sh} decreases the resonance and anti-resonance frequencies, i.e., the local minimum and local maximum frequencies respectively, with small changes in magnitude. Decreasing C_{sh} increases the resonance and anti-resonance frequencies. The same trends are observed for C_g variation. It will be seen that the impact of varying C_g and C_{sh} is more pronounced at frequencies above 400 kHz.

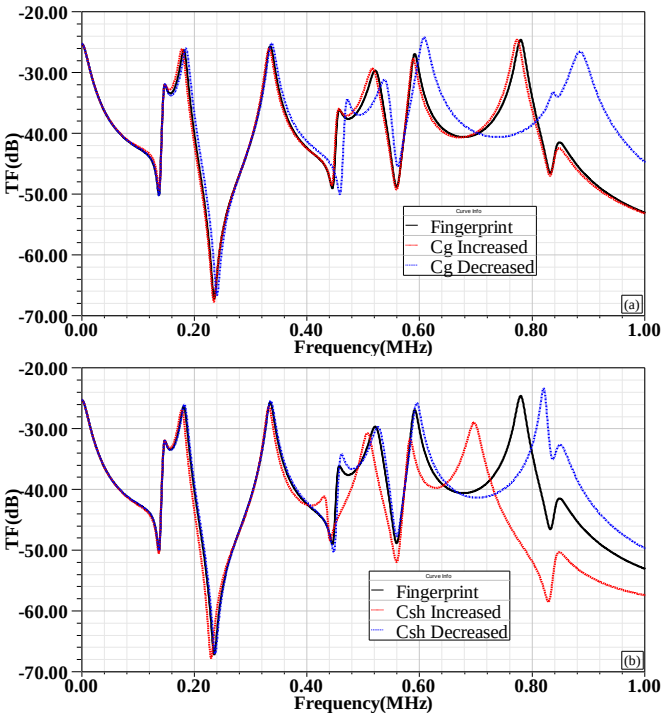

Fig. 3. Effect of ± 10% changes in the HV capacitance on the FRA signature, relative to the baseline (a) C_g, (b) C_{sh}

Fig. 4 shows the effect of changing the self (L_s) and mutual (M_{ij}) inductances by ±10%. Unlike the effect of changes in C_g and C_{sh}, which appears at frequencies above 400 kHz, the effect of changes in L_s and M_{ij} appears below 20 kHz and is more pronounced close to 1 MHz. This is attributed to the fact that the amount of magnetic flux penetrating the transformer core at low frequencies is significant, so that the core characteristics affect the FRA signature at low frequency. At high frequencies the magnetic flux tends to encase the core and the transformer capacitive components dominate the response.

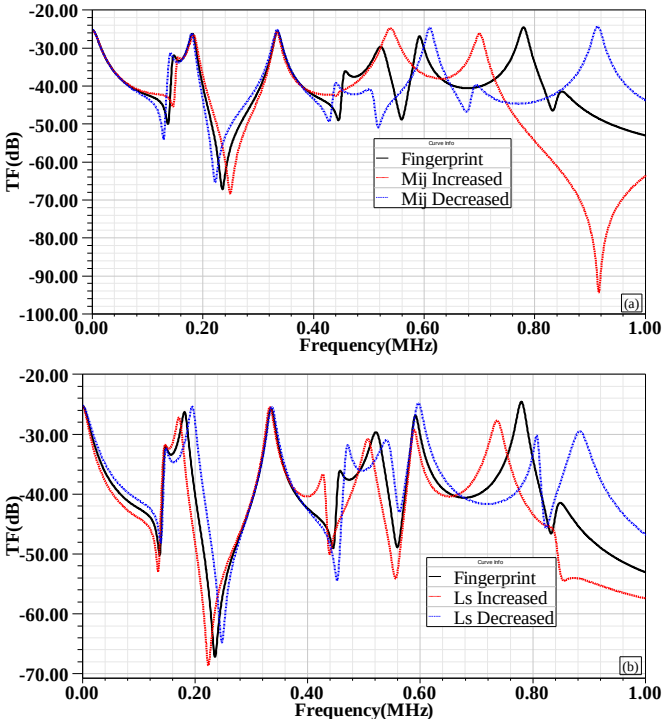

Fig. 4. Effect of ± 10% changes in the HV self/mutual inductances on the FRA signature, relative to the baseline (a) mutual inductance M_{ij} (b) self inductance L_S

As shown in Fig. 4, increasing L_s decreases the resonance and anti-resonance frequencies, with small changes in magnitude. On the other hand, decreasing L_s increases the resonance and anti-resonance frequencies, again with small changes in magnitude. Opposite trends are observed when the mutual inductances M_{ij} are changed, i.e., increasing M_{ij} increases the resonance and anti-resonance frequencies, and decreasing M_{ij} decreases them, over the entire frequency range.

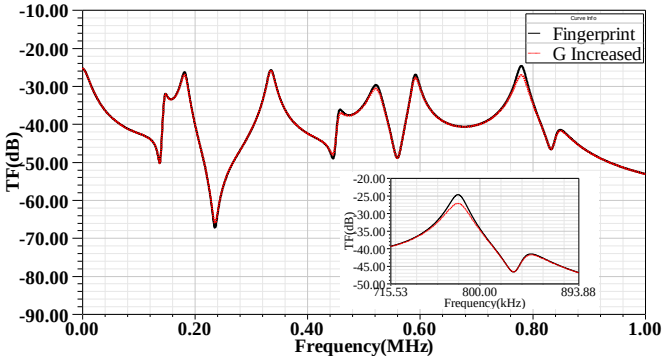

Fig. 5. Effect of increased dielectric conductance G on the FRA signature

Fig. 5 shows the effect increasing the HV conductance (G) by 10% on the FRA signature (A decrease in conductance, i.e., an increase in dielectric resistance, is considered unlikely for transformer insulation). As shown in Fig. 5, increasing the dielectric conductance (G) has no effect on the resonance and anti-resonance frequencies. It does however slightly change the magnitudes of the peaks at high frequencies. This result is attributed to the very high dielectric resistance used in the simulation (7 MΩ), typical for transformer oil.

The effects of ±10% variations in various electrical parameters on the FRA resonance frequencies and magnitudes are summarised in Table III.

TABLE III
EFFECTS OF ±10% VARIATIONS IN VARIOUS ELECTRICAL PARAMETERS ON FRA REONANCE FREQUENCIES AND MAGNITUDES (RELATIVE TO FINGERPRINTS)

Parameter Variations		**Frequency Range**		
		Low (<20 kHz)	**Medium (20–400 kHz)**	**High (>400 kHz)**
L_s	10% Increase	Magnitude and resonance frequencies decreased	Magnitude and resonance frequencies decreased	Magnitude and resonance frequencies decreased
	10% Decrease	Magnitude and resonance frequencies increased	Magnitude and resonance frequencies increased	Magnitude and resonance frequencies increased
C_{sh}	10% Increase	No impact	No impact	Resonance frequencies, magnitude decreased
	10% Decrease	No impact	No impact	Resonance frequencies, magnitude increased
C_g	10% Increase	No impact	No impact	Resonance frequencies slightly decreased
	10% Decrease	No impact	No impact	Resonance frequencies, magnitude increased
M_{ij}	10% Increase	Resonance frequencies increased	Resonance frequencies increased	Resonance frequencies increased
	10% Decrease	Resonance frequencies decreased	Resonance frequencies decreased	Resonance frequencies decreased
G	10% Increase	No impact	No impact	Magnitude decreased

IV. FAULT ANALYSIS

In order to simulate physical faults within the transformer, Simplorer and Maxwell software were used to simulate a 3D finite element model of the single phase, shell-type transformer shown in Fig. 6.

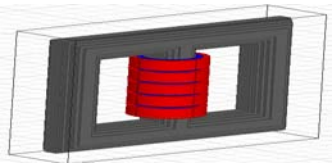

Fig. 6. 3D Transformer model

Various mechanical faults within the transformer model were simulated by changing the transformer coil configuration. The corresponding changes in the electrical parameters of the transformer model (Fig. 2) were calculated using the software. The resulting signatures were compared with the fingerprint signature.

A. Loss of Clamping Pressure

Loss of clamping pressure is a common problem, particularly in aged transformers. It is caused by mechanical hysteresis in pressboard and paper insulation [24], and leads to an increase in insulation conductivity because of the reduced insulation thickness between winding layers. It can be simulated by increasing the value of the shunt conductance G_{sh} [21]. Figs. 7 and 8 show the effect of a 20% increase in G_{sh} on the FRA signatures of the HV and LV windings respectively; the resonance and anti-resonance frequencies are not shifted, but the magnitudes of the resonance peaks are decreased over the entire frequency range. The large negative spike in the HV winding signature around 200 kHz is thought to be an artefact of the software.

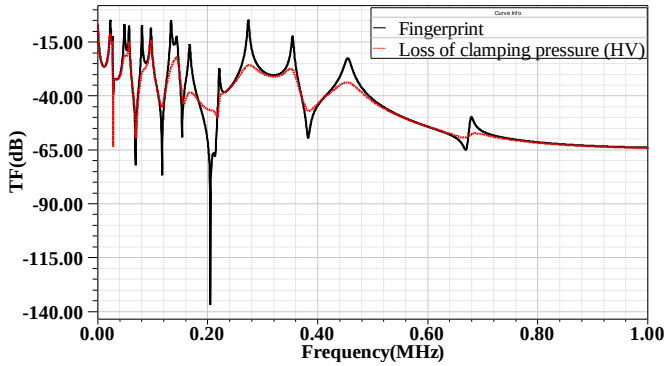

Fig. 7. Effect of simulated loss of clamping pressure on the FRA signature of the HV winding

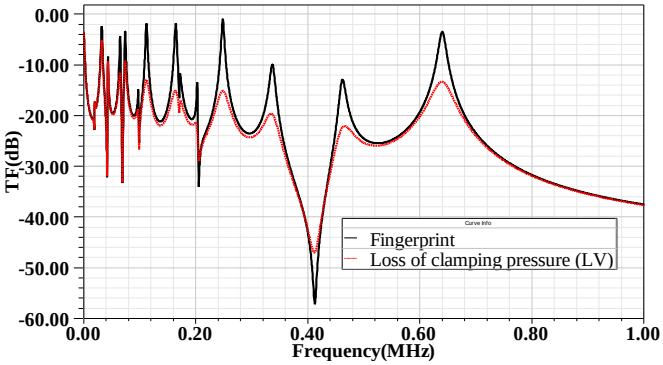

Fig. 8. Effect of simulated loss of clamping pressure on the FRA signature of the LV winding

B. Inter-Disk Fault

The inter-disk fault is one of the most common mechanical faults within power transformers, and approximately 80% of mechanical failures are attributable to it [12]. It is due to changes in the axial disk space (Fig.9) caused by excess mechanical stress and short circuit faults, and can be simulated by increasing the series capacitance (C_{sh}) and the mutual inductance (M_{ij}) between the two relevant disks [25, 26]. Fig. 10 shows the effect of a 10% increase in C_{sh} and M_{ij} on the HV FRA signature when the fault occurs at the top, middle and bottom of the HV winding. A 10% increase in C_{sh} and in M_{ij} corresponds to a 10% increase in Δh, the space between the affected disks (Fig. 9). Fig. 10 shows that this fault does not have a significant effect on the FRA signature at frequencies below 300 kHz. The resonance and anti-resonance frequencies above 300 kHz are decreased, and the peak magnitudes are changed. The frequency decreases are larger when the fault occurs within the top or bottom disks of the winding, rather than within the middle disks.

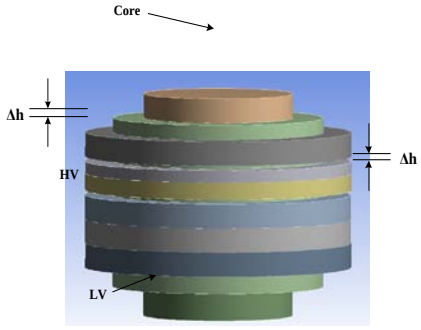

Fig. 9. Interdisk fault (Δh) configuration

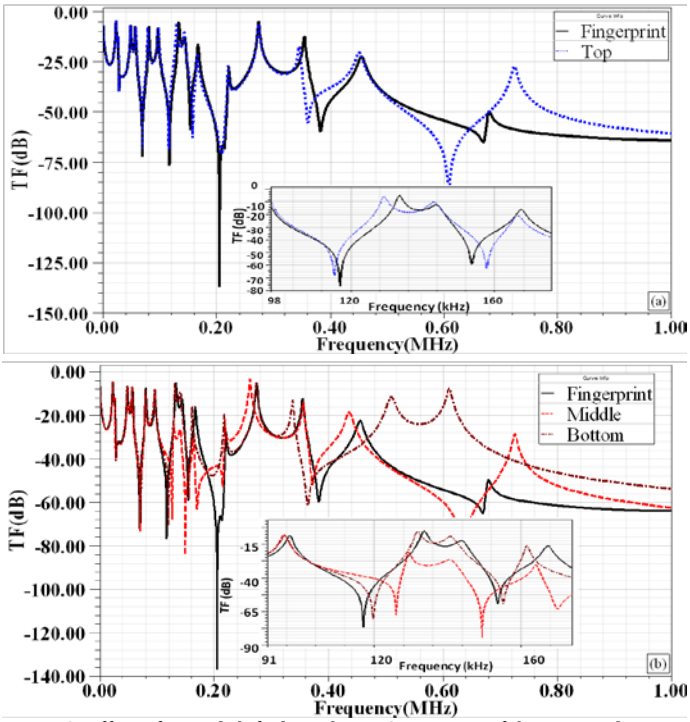

Fig. 10. Effect of inter-disk fault on the FRA signature of the HV winding.

C. HV Winding Bushing Fault

This type of fault can be simulated by connecting the bushing T-circuit model shown in Fig. 11 between the voltage source V_{in} and the transformer model shown in Fig. 2 [5].

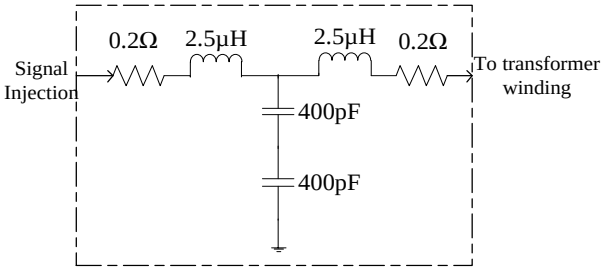

Fig. 11. Transformer bushing model [5]

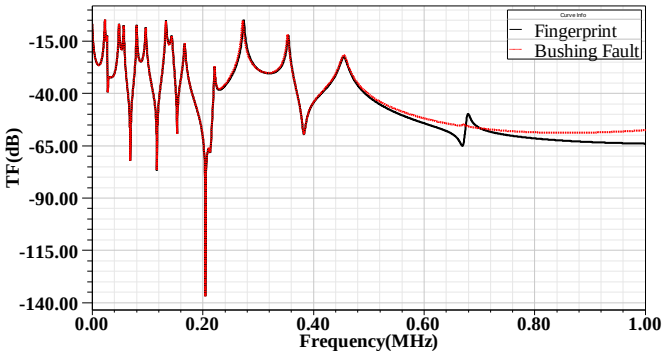

Fig. 12. Impact of high voltage bushing fault on the FRA signature of the HV winding

The effect of a 10% reduction in bushing capacitance (800 pF) shown in Fig. 11 on the FRA signature is shown in Fig. 12. A reduction in bushing capacitance corresponds to a reduction in the breakdown voltage of the bushing insulation. As shown in Fig. 12, there is no significant change in the signature below 600 kHz, but the resonance and antiresonance peaks around 700 kHz in the fingerprint disappear.

D. Axial Displacement Fault

This fault occurs due to imbalanced magnetic forces generated in a winding as a result of a short-circuit fault [21]. These forces cause axial movement of the winding as shown in Fig. 13.

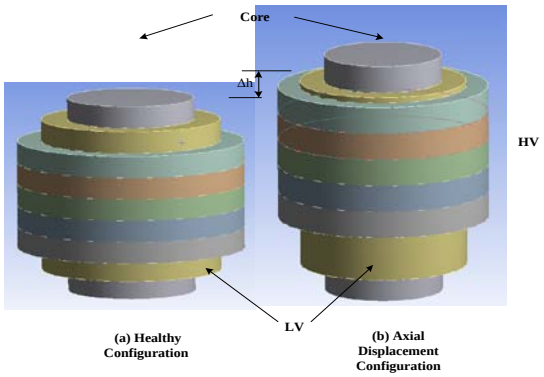

Fig. 13. Axial displacement (Δh) configuration

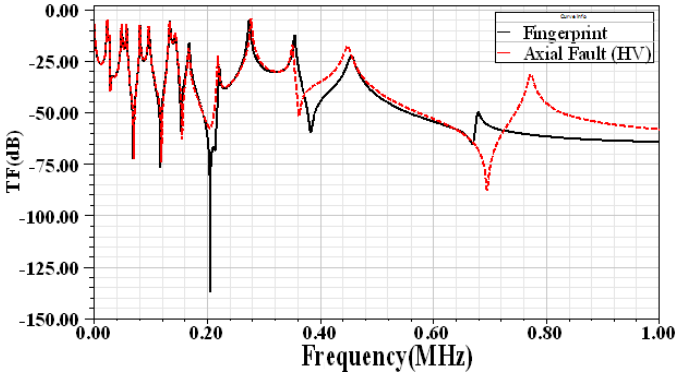

Fig. 14. Impact of HV axial displacement on the FRA signature

The fault can be simulated by changing the values of the series capacitance (C_{sh}) and mutual inductance (M_{ij}) between the HV and LV windings [27]. A 10% increase in C_{HL} and in M_{ij} corresponds to approximately 10% movement Δh which is the ratio of the HV axial displacement and the overall length of the winding (Fig. 13).

Fig. 14 shows that such a fault has little effect on the FRA signature below 200 kHz. In the range 200-400 kHz the resonance frequencies and magnitudes decrease. The resonance around 700 kHz in the fingerprint is shifted towards higher frequency and its magnitude increases. These trends are independent of the direction of the axial movement.

E. Dielectric Leakage Current Fault

Ground shield damage, oil and paper aging, high moisture content in the winding and abrasion of solid insulation are the main causes of leakage current to earth through transformer insulation [28]. This type of fault can be simulated by increasing the conductance between the HV winding and the ground (G in Fig.2) [29]. Fig. 15 shows that this fault produces small changes in peak magnitude below 200 kHz.

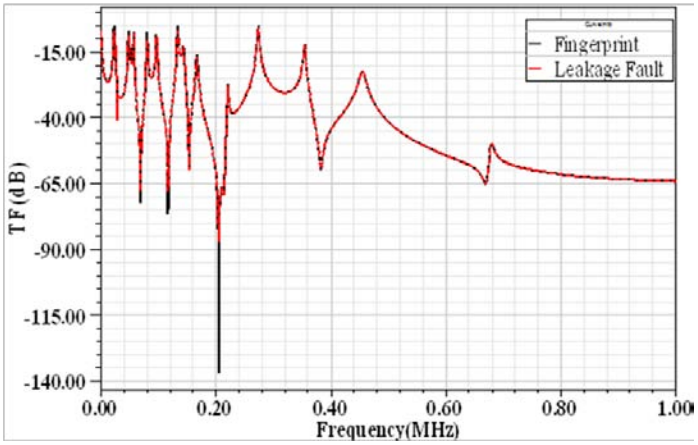

Fig. 15. Effect of leakage fault on the FRA signature

F. Short Circuit Fault

This fault is due to erosion of the winding and conductor insulation, due to vibrations generated by electromechanical forces. The erosion may lead to excessive current in the winding [27]. The fault can be simulated by short circuiting the series resistance R_s and the series inductance L_s of the HV winding (Fig.2) [30]. Fig. 16 shows that it fault has little effect on the signature at frequencies below 200 kHz. At higher frequencies the magnitude is slightly increased and the resonance frequencies are slightly decreased. The same fault has a greater effect when it occurs at the top or bottom of the winding rather than in the middle.

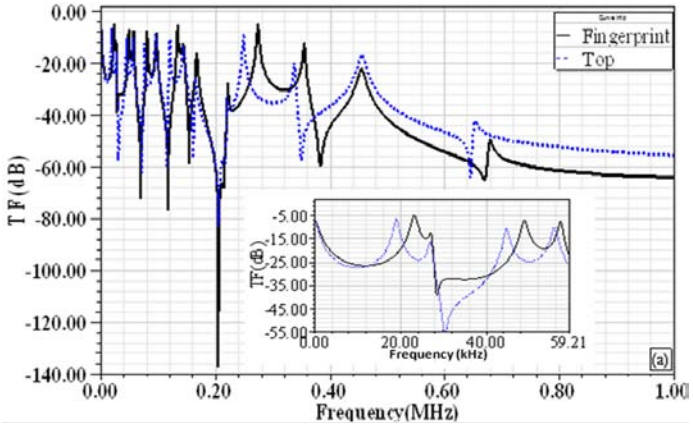

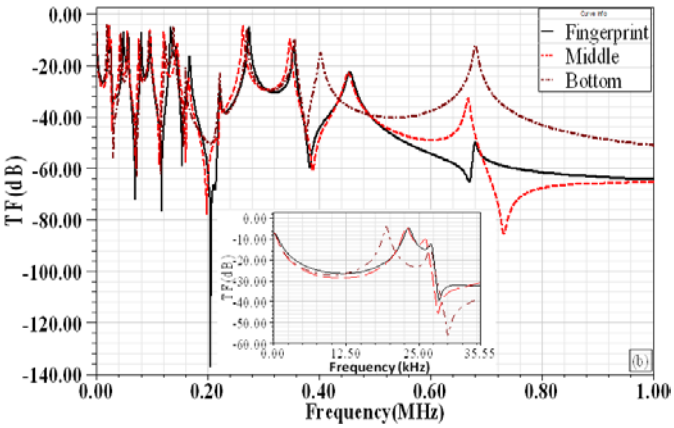

Fig. 16. Impact of HV winding short circuit fault on the FRA signature when it occurs (a) at the top of the winding, (b) at the middle and bottom of the winding

G. Radial Displacement Fault

Windings may be subjected to radial forces arising from the interaction of the winding current with the magnetic flux. Fig.17 shows a radial dislocation between the LV and HV windings. Large radial forces may lead to winding buckling [31]. This fault can be simulated by decreasing the capacitance to ground (C_g), the capacitance between the HV and LV windings (C_{HL}), and the mutual inductance (M_{ij}) of the impacted disks [32]. A simultaneous decrease of 10% in each of these three parameters corresponds to a 10% radial displacement Δw of the impacted disks as shown in Fig. 17. Δw is calculated as the ratio of the radial displacement of the impacted disks to the diameter of the disk. The FRA responses of the HV and LV windings are shown in Fig. 18 (a) and (b) respectively.

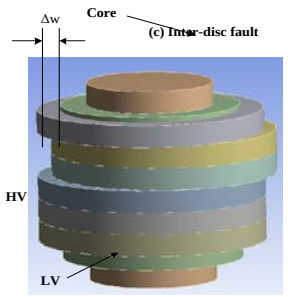

Fig. 17. Radial fault (Δw) configuration

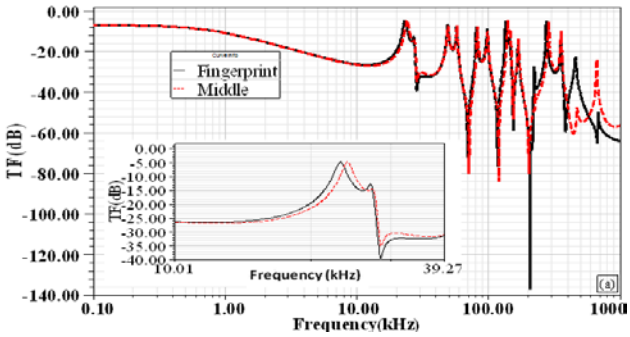

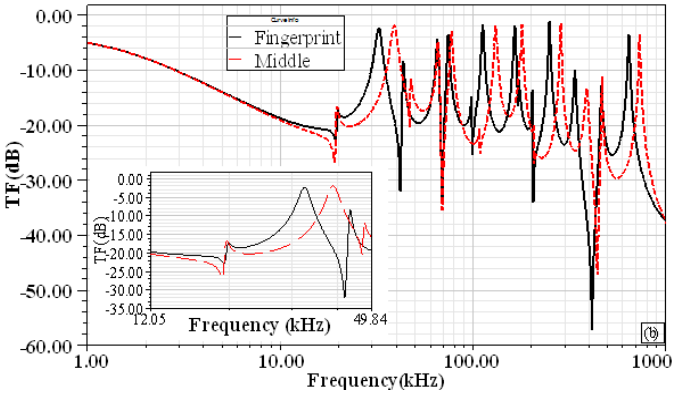

Fig. 18. Impact of radial fault on the FRA signature (a)HV (b) LV winding

Fig. 18 (a) shows that the resonance frequencies of the HV winding are increased slightly at frequencies above 400 kHz. In the LV winding an increase occurs at frequencies above 20 kHz.

Table IV is a listing of the various fault types and their effects on the FRA signature. It could be used in the formulation of standard codes for power transformer FRA signature interpretation.

TABLE IV
IMPACT OF VARIOUS FAULTS ON TRANSFORMER FRA SIGNATURE

Fault Type	**Frequency Range**		
	< 20kHz	**20-400 kHz**	**> 400 kHz**
Axial Displacement	No impact	Resonance frequencies and magnitude decreased	Resonance frequencies and magnitude increased
Radial Displacement	Resonance frequencies increased	Resonance frequencies increased	Resonance frequencies increased
High Voltage Bushing	No impact	No impact	Magnitude decreased, one resonance frequency disappears
Dielectric Leakage current	Magnitude decreased	Magnitude decreased	No impact
Inter Disk	No significant impact	Resonance frequencies and magnitudes increased	Resonance frequencies and magnitudes increased
Short Circuit	No significant impact	Resonance frequencies decreased and magnitudes increased	Resonance frequencies decreased and magnitudes increased
Loss of Clamping Pressure	Magnitude decreased	Magnitude decreased	Magnitude decreased

V. CONCLUSION

This paper presents a comprehensive analysis of the effects of various faults on the FRA signatures of a transformer simulated by a high frequency model. The faults were simulated through changes in the values of some of the electrical components in the model. It was found that radial displacement of a winding alters the FRA signature over the entire frequency range (10 Hz-1 MHz), whereas changes due

to axial displacement occur only at frequencies above 200 kHz. A table listing various transformer faults and the associated changes in the FRA signature was compiled, and could be used in the formulation of standard codes for power transformer FRA signature interpretation.

APPENDIX

TRANSFORMER MODEL COMPONENT VALUES [9, 13]

	R_s	L_s	C_{sh}	C_g	C_{hl}	$1/G$
HV	1.2Ω	180μH	0.013nF	3nF	5nF	7 MΩ
LV	0.5Ω	65μH	0.026nF	6nF	5Nf	7 MΩ

VI. REFERENCES

[1] S. Islam, K. M. Coates, and G. Ledwich, "Identification of high frequency transformer equivalent circuit using Matlab from frequency domain data," in Industry Applications Conference, 1997. Thirty-Second IAS Annual Meeting, IAS '97., Conference Record of the 1997 IEEE, 1997, pp. 357-364 vol.1.

[2] E.J. Figueroa,"Managing An Aging Fleet of Transformers," Canada, 2009.

[3]L. M. Geldenhuis, "Power transformer life management," in Electricity Distribution, 2005. CIRED 2005. 18th International Conference and Exhibition on, 2005, pp. 1-4.

[4]S. M. Islam and G. Ledwich, "Locating transformer faults through sensitivity analysis of high frequency modeling using transfer function approach," in Electrical Insulation, 1996., Conference Record of the 1996 IEEE International Symposium on, 1996, pp. 38-41 vol.1.

[5]M. Wang, A. J. Vandermaar, and K. D. Srivastava, "Improved detection of power transformer winding movement by extending the FRA high frequency range," Power Delivery, IEEE Transactions on, vol. 20, pp. 1930-1938, 2005.

[6]W. J. McNutt, W. M. Johnson, R. A. Nelson, and R. E. Ayers, "Power Transformen Short-Circuit Strength - Requirements, Design, and Demonstration," Power Apparatus and Systems, IEEE Transactions on, vol. PAS-89, pp. 1955-1969, 1970.

[7]M. Bagheri, M. S. Naderi, T. Blackburn, and T. Phung, "FRA vs. short circuit impedance measurement in detection of mechanical defects within large power transformer," in Electrical Insulation (ISEI), Conference Record of the 2012 IEEE International Symposium on, 2012, pp. 301-305.

[8]K. G. N. B. Abeywickrama, Y. V. Serdyuk, and S. M. Gubanski, "Exploring possibilities for characterization of power transformer insulation by frequency response analysis (FRA)," Power Delivery, IEEE Transactions on, vol. 21, pp. 1375-1382, 2006.

[9]E. Rahimpour, M. Jabbari, and S. Tenbohlen, "Mathematical Comparison Methods to Assess Transfer Functions of Transformers to Detect Different Types of Mechanical Faults," Power Delivery, IEEE Transactions on, vol. 25, pp. 2544-2555, 2010.

[10]B. J. Small and A. Abu-Siada, "A new method for analysing transformer condition using frequency response analysis," in Power and Energy Society General Meeting, 2011 IEEE, 2011, pp. 1-5.

[11]S. D. Mitchell and J. S. Welsh, "Modeling Power Transformers to Support the Interpretation of Frequency-Response Analysis," Power Delivery, IEEE Transactions on, vol. 26, pp. 2705-2717, 2011.

[12]E. Rahimpour, J.Christian, K. Feser, H. Mohseni, "Transfer Function Method to Diagnose Axial Displacement, Radial Deformation of Transformer Winding," Power Engineering Review, IEEE, vol.22, pp.70-70, 2002.

[13] C. A. Platero, F. Blazquez, P. Frias, and D. Ramirez,"Influence of Rotor Position in FRA Response for Detection of Insulation Failures in Salient-Pole Synchronous Machines," *IEEE Transactions on Energy Conversion*, vol. 26, pp. 671-676, June 2011.

[14]E. P. Dick and C. C. Erven, "Transformer Diagnostic Testing by Frequuency Response Analysis," Power Apparatus and Systems, IEEE Transactions on, vol. PAS-97, pp. 2144-2153, 1978.

[15]W. Zhongdong, L. Jie, and D. M. Sofian, "Interpretation of Transformer FRA Responses— Part I: Influence of Winding Structure," Power Delivery, IEEE Transactions on, vol. 24, pp. 703-710, 2009.

[16]A. Shintemirov, W. H. Tang, and Q. H. Wu, "Transformer winding condition assessment using frequency response analysis and evidential reasoning," Electric Power Applications, IET, vol. 4, pp. 198-212, 2010.

[17]E. Rahimpour, J. Christian, K. Feser, H. Mohseni,"Transfer function method to diagnose axial displacement and radial deformation of transformer windings," Power Delivery, IEEE Transactions on, vol. 18, pp.493-505, 2003.

[18]L. Satish and S. K. Sahoo, "An effort to understand what factors affect the transfer function of a two-winding transformer," Power Delivery, IEEE Transactions on, vol. 20, pp. 1430-1440, 2005.

[19]K. Ragavan and L. Satish, "Localization of Changes in a Model Winding Based on Terminal Measurements: Experimental Study," Power Delivery, IEEE Transactions on, vol. 22, pp. 1557-1565, 2007.

[20]A. Shintemirov, W. H. Tang, and Q. H. Wu, "Transformer Core Parameter Identification Using Frequency Response Analysis," Magnetics, IEEE Transactions on, vol. 46, pp. 141-149, 2010.

[21]A. Abu-siada and S. Islam, "A Novel Online Technique to Detect Power Transformer Winding Faults," Power Delivery, IEEE Transactions on, vol. 27, pp. 849-857, 2012.

[22]A. A. Reykherdt and V. Davydov, "Case studies of factors influencing frequency response analysis measurements and power transformer diagnostics," Electrical Insulation Magazine, IEEE, vol. 27, pp. 22-30, 2011.

[23]N. Abeywickrama, Y. V. Serdyuk, and S. M. Gubanski, "High-Frequency Modeling of Power Transformers for Use in Frequency Response Analysis (FRA)," Power Delivery, IEEE Transactions on, vol. 23, pp. 2042-2049, 2008.

[24]G. Junfeng, G. Wensheng, T. Kexiong, and G. Shengyou, "Deformation analysis of transformer winding by structure parameter," in Properties and Applications of Dielectric Materials, 2003. Proceedings of the 7th International Conference on, 2003, pp. 487-490 vol.1.

[25]D. M. Sofian, W. Zhongdong, and L. Jie, "Interpretation of Transformer FRA Responses— Part II: Influence of Transformer Structure," Power Delivery, IEEE Transactions on, vol. 25, pp. 2582-2589, 2010.

[26]E. Rahimpour, S. Tenbohlen, "Experimental and theoretical investigation of disc space variation in real high-voltage windings using transfer function method," Electric Power Applications, IET, vol. 4, pp. 451-461, 2010.

[27] M.R.Barzegaran, "Detecting the Position of Winding Short Circuit Faults in Transformer using High Frequency Analysis," European Journal of Scientific Research ISSN 1450-216X Vol.23 No.4 (2008), pp.644-658, 2008

[28]N. Abeywickrama, Y. V. Serdyuk, and S. M. Gubanski, "Effect of Core Magnetization on Frequency Response Analysis (FRA) of Power Transformers," Power Delivery, IEEE Transactions on, vol. 23, pp. 1432-1438, 2008.

[29]J. Chong and A. Abu-Siada, "A novel algorithm to detect internal transformer faults," in Power and Energy Society General Meeting, 2011 IEEE, 2011, pp. 1-5.

[30]J. Bak-Jensen, B. Bak-Jensen, and S. D. Mikkelsen, "Detection of faults and ageing phenomena in transformers by transfer functions," Power Delivery, IEEE Transactions on, vol. 10, pp. 308-314, 1995.

[31]K. Pourhossein, G. B. Gharehpetian, and E. Rahimpour, "Buckling severity diagnosis in power transformer windings using Euclidean Distance classifier," in Electrical Engineering (ICEE), 2011 19th Iranian Conference on, 2011, pp. 1-1.

[32]W. H. Tang, A. Shintemirov, and Q. H. Wu, "Detection of minor winding deformation fault in high frequency range for power transformer," in Power and Energy Society General Meeting, 2010 IEEE, 2010, pp. 1-6.

A. Abu-Siada (M'07, SM'12) received his B.Sc. and M.Sc. degrees from Ain Shams University, Egypt and the PhD degree from Curtin University, Australia, all in Electrical Engineering. Currently he is a Senior Lecturer in the Department of Electrical and Computer Engineering at Curtin University. His research interests include power system stability, condition monitoring, power electronics and power quality. He is Editor-in-Chief of the international journal Electrical and Electronic Engineering, a regular reviewer for IEEE Transactions on Dielectrics and Electrical Insulation, Power Electronics and Sustainable Energy. He is the vice-chair of the IEEE Computation Intellegence Society, WA Chapter.

N. Hashemnia received BSc in Electrical Power Engineering from Yazd University, Iran in 2006 and Master of Electrical Utility Engineering from Curtin University in 2010. He received a scholarship from the Cooperative Research Centre for Infrastructure and Asset Management in August 2011, to enable him to pursue his PhD study at Curtin University. His research interests include power transformer condition monitoring and application of artificial intelligence to power systems.

S. Islam (M'83, SM'93) received the B.Sc. from Bangladesh University of Engineering and Technology, Bangladesh, and the M.Sc. and PhD degrees from King Fahd University of Petroleum and Minerals, Saudi Arabia, all in electrical power engineering, in 1979, 1983, and 1988 respectively. He is currently the Chair Professor in Electrical Power Engineering at Curtin University, Australia. He received the IEEE T

Burke Haye Faculty Recognition award in 2000. His research interests are in condition monitoring of transformers, wind energy conversion and power systems. He is a regular reviewer for the IEEE Transactions on Energy Conversion, Power Systems and Power Delivery. Prof. Islam is an Editor of the IEEE Transaction on Sustainable Energy.

Mohammad A. S. Masoum (S'88–M'91–SM'05) received his B.S., M.S. and Ph.D. degrees in Electrical and Computer Engineering in 1983, 1985, and 1991, respectively, from the University of Colorado, USA. Dr. Masoum's research interests include optimization, power quality and stability of power systems/electric machines and distributed generation. Currently, he is a Professor and the Discipline Leader and Course Coordinator for Power System Engineering in the Electrical and Computer Engineering Department, Curtin University, Australia. He is the co-author of *Power Quality in Power Systems and Electrical Machines* (Elsevier, 2008) and *Power Conversion of Renewable Energy Systems* (Springer, 2011). Dr. Masoum is Editor-in-Chief for the American Journal of Engineering and Applied Science, and an editor of the Australian Journal of Electrical & Electronic Engineering.

Food Volume Estimation in a Mobile Phone Based Dietary Assessment System

M. H. Rahman[a], Q. Li[a], M. R. Pickering[a], M. R. Frater[a], D. A. Kerr[b]
[a]School of Engineering & Information Technology
The University of New South Wales
Canberra, Australia
e-mail: md.rahman2@student.adfa.edu.au

[b]School of Public Health
Curtin University
Perth, Australia

C. J. Bouchey[c], E. J. Delp[d]
[c]University of Hawaii Cancer Center
University of Hawaii
Hawaii, USA

[d]School of Electrical and Computer Engineering
Purdue University
West Lafayette, USA
e-mail: ace@ecn.purdue.edu

Abstract— There is now convincing evidence that poor diet, in combination with physical inactivity are key determinants of an individual's risk of developing chronic diseases, such as obesity, cancer, cardiovascular disease or diabetes. Assessing what people eat is fundamental to establishing the link between diet and disease. Food records are considered the best approach for assessing energy intake. However, this method requires literate and highly motivated subjects and adolescents and young adults are the least likely to undertake food records. The ready access of the majority of the population to mobile phones has opened up new opportunities for dietary assessment. In such systems, the camera in the mobile phone is used for capturing images of food consumed and these images are then processed to automatically estimate the nutritional content of the food. A vital step in this process is the estimation of the volume of the food in the image. In this paper we propose a food volume estimation approach which requires only a stereo pair of images to be captured. Our experimental results show that the proposed approach can provide an accurate estimate of the volume of typical food items in a passive manner without the need for manual fitting of 3D models to the food items.

Keywords- dietary assessment; food records; feature detection; volume estimation; disparity map; depth map

I. INTRODUCTION

Preventing disease through improving nutrition is a global health priority [1]. Approximately 30% of all cancers have been attributed to dietary factors [2]. The strongest evidence for diet increasing cancer risk is specifically with overweight and obesity, high consumption of alcoholic beverages, aflatoxins and fermented foods. A diet of at least 400 g per day of fruits and vegetables appears to decrease cancer risk. However, a key barrier to linking dietary exposure and disease is the ability to measure dietary factors, including intake of food groups such as fruits and vegetables, with specificity and precision [3].

Assessing what people eat is fundamental to establishing the link between diet and disease. However, it is now more challenging to do this as consumers have moved away from eating a traditional 'meat and 3-veg' meal at home to purchasing more take-away food and eating out [4, 5]. With this greater proportion of foods eaten away from home [6, 7], it is now becoming increasingly difficult for consumers to accurately assess how much they have eaten or the composition of their meal.

Food records are considered the best approach for assessing energy intake (kilojoules). With a paper-based food record, subjects are asked to record their food and fluid intake for between 3-7 days. This method requires literate and highly motivated subjects. Research has shown adolescents and young adults, who typically have unstructured eating habits and frequently snack, are the least likely to undertake food records [8].

With advances in technology it is now timely to explore how mobile devices can better capture food intake in real-time by potentially reducing the burden of the recording task to both the subject and the researcher. The ready access of the majority of the population to mobile phones has opened up new opportunities for dietary assessment which are yet to be leveraged. Tufano et al. [9] in a review of eHealth (web and mobile phone) applications refers to this as 'technology convergence' in which real-time or near-real time multimedia communication capabilities can occur.

The integrated camera in the mobile phone is used for capturing images of food consumed. These images are then processed to automatically estimate the nutritional content of the food items for record keeping purposes and to provide feedback to the patient. To estimate the nutritional content of food items in an image the food item must be recognized and the mass of the food item must be estimated. A vital step in estimating the mass of the food item is to estimate its volume as this can then be used in conjunction with a density database of food items to estimate the mass of the food in the image. Previous approaches to volume estimation of food have included passive and active approaches which require the user to capture form one image up to several pairs of images of the food item.

Shang et al. [10, 11] proposed an active approach to food volume estimation using structured light. In their proposed system a laser module is attached to a mobile phone. This module produces a rectangular grid pattern with the brightness of the lines decreasing according to the distance from the center of the pattern. Grid lines are extracted from the camera image and a depth map is created from multiple pairs of images after a calibration stage. This depth map can be used to create a 3D surface

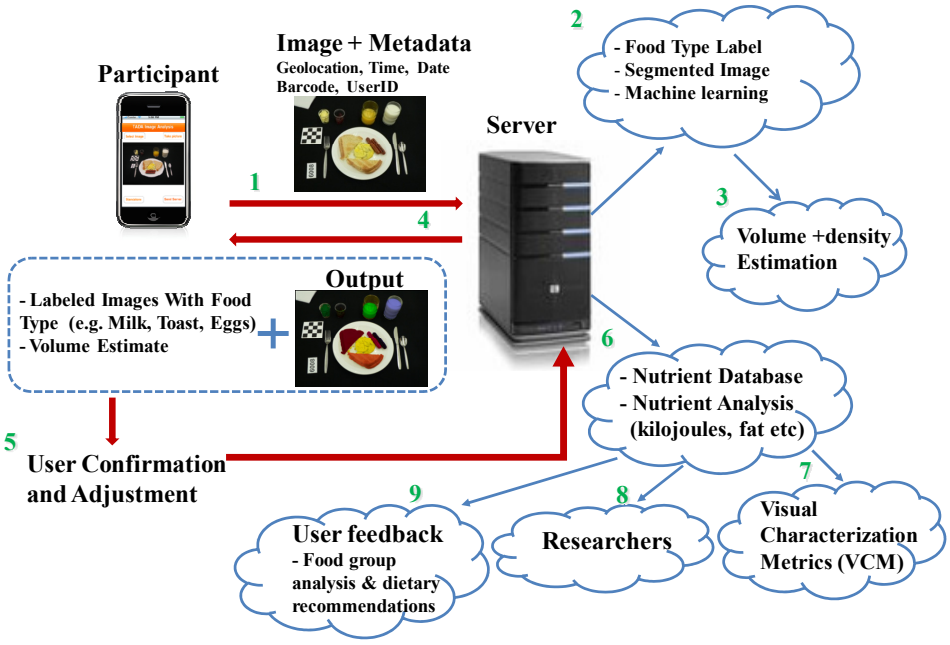

Figure 1. System architecture for the TADA dietary assessment system.

and the volume inside this surface is taken as the volume of the food item.

Martin et al. [12] proposed a system to estimate volume based on a single image of the food. They assumed that the foods captured in the image are approximately bowl-shaped and inferred the volume of the food item from the surface area of the food. They essentially use a predefined linear relationship between surface area and volume. This technique relies on the validity of the bowl shape assumption and is relatively inaccurate for foods that do not satisfy this assumption (spherical fruit for example).

Weiss et al. [13] used a system that required three images of the food item and a calibration grid pattern. This allowed the height of the food item above a reference plane to be estimated and from this height the volume of the food between this 3D surface and the plate was estimated. The requirement to capture three images was a disadvantage of this system as this is considered to be overly burdensome to the participants.

Chen et al. [14] proposed a system that requires only a single image of the food item. The user then manually selects one of a number of predefined geometric models such as a cube, sphere etc. A 3D/2D registration step then automatically aligns the 3D model to the 2D projection of the food item in order to estimate the scale and pose o the 3D model which best matches the 2D projection of the food item. After calibration, the volume of the 3D model at the registered pose and scale is taken as the volume of the food item. This reported estimation errors for this technique were approximately 5% for food items which had a shape that matched one of the pre-defined models and 10% for irregularly shaped objects.

Woo et al. [15] proposed a similar approach which also included irregularly shaped 3D models which consisted of the surface shape of the food item extended towards the surface of the plate to create an irregular prismatic model of the food item. They also allowed manual refinement of the 3D model where the user defined the distance to extend the prismatic model. Chae et al. [16] used 3D model templates for specific common food items including liquids in clear near-cylindrical containers and bread slices. The proposed techniques provided a method for automatically determining the 3D shape of these specific food items (by automatically determining the thickness of the slice of bread on a plate for example).

In this paper we propose a food volume estimation approach similar to that proposed by Weiss et al.. However our proposed approach requires only a stereo pair of images to be captured. The proposed approach also includes a novel slice based estimation approach to estimate the volume of a food item from a partial point cloud of the surface of the food item. The proposed approach can be used to estimate the volume of any irregularly shaped food item.

II. The Mobile Phone Based Dietary Assessment System

The food volume estimation procedure proposed in this paper will be utilized in the mobile phone based dietary assessment system that has been developed as part of the Technology Assisted Dietary Assessment (TADA) project. The system architecture for this system is shown in Figure 1. The users of the system are given a mobile phone with a built-in camera, network connectivity, and integrated image analysis and visualization tools to allow their food and beverage intake to be recorded. The process starts with the user sending the food image and contextual metadata (date, time, geo-location, etc.) to the server via the data network (step 1). The user places a fiducial marker in each image that allows the images to be spatially and color

calibrated. Food identification (and in the future volume and density estimation) is performed on the server (steps 2 and 3) for finding the nutrient information (step 6). The database contains information on the most commonly consumed foods, their nutrient values, and weights and densities for typical food portions. The food database uses image based features, referred to as Visual Characterization Metrics (VCMs) (step 7), to index the nutrient information. Finally, these results are sent to the researcher for further analysis (step 8) and future developments will incorporate user feedback including food group analysis and dietary recommendations (step 9).

III. 3D Reconstruction of Food Items

In order to estimate the volume of any food object in the image based dietary assessment system, firstly we need to reconstruct the 3D shape of the food. The three dimensional (3D) reconstruction of objects from single/multiple view/s is an on-going research area in the field of computer vision. Humans interpret depth using various visual cues to understand the third dimension of an object, in the 3D world. However, for a given two dimensional (2D) image, we have the ability to visualize the third dimension through information on perspective projection from the images. The interest lies in the process of gathering this 2D image data and processing it to create the 3D structure. Hence, 3D reconstruction involves the use of techniques in computer vision to add the missing dimension to create the 3D space from 2D images.

To describe the process of mage acquisition we will use the pinhole camera model, which projects 3D objects onto a 2D image plane. We will then introduce the basic geometry used for the reconstruction of points in 3D space using two different (calibrated) camera viewpoints. Finally, a simple algorithm which can be used to recover the 3D position of such points from their 2D views will be explained.

A. Pinhole Camera Model

A point in 3D space $w=[X, Y, Z]^T$ and its projection in a 2D image plane $m=[x, y]^T$ can be represented using the pinhole camera model as shown in Figure 2(a). The relationship of the projection between the two planes can be expressed using the homogeneous coordinate:

$$\tilde{m} = M\tilde{w} \tag{1}$$

Here M is the perspective projection matrix which can be represented as

$$M = K[R \mid t] \tag{2}$$

K is the camera matrix containing internal parameters, given by

$$K = \begin{bmatrix} \alpha & s & x_0 \\ 0 & \beta & y_0 \\ 0 & 0 & 1 \end{bmatrix} \tag{3}$$

where $\alpha = fk_x$, $\beta = fk_y$, f is the focal length, k_x and k_y are the distortions along the image plane, s is the skew factor, and (x_0, y_0) is the principal point, i.e. the point where the optical axis intersects with the image plane.

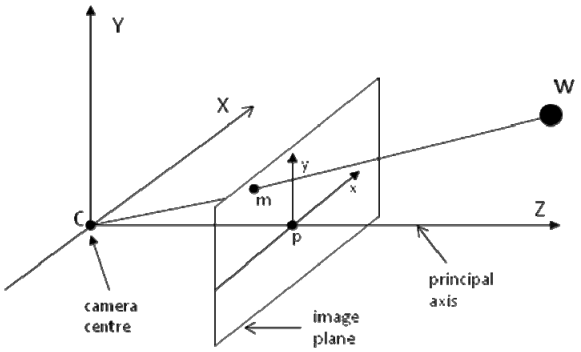

(a) Pinhole camera model

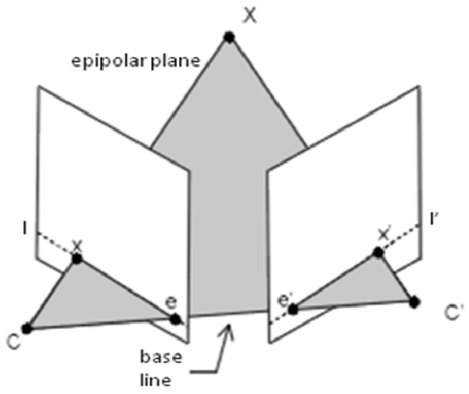

(b) Epipolar geometry

Figure 2. Camera and projection

B. Epipolar Geometry

Epipolar geometry refers to the intrinsic projective geometry between two views. It is independent of the structure in the scene and only depends on the cameras' intrinsic parameters and relative positions. Suppose a point X in 3D space is captured by two views, at x in the left view and x' in the right view as shown in Figure 2(b). Then image points x and x', space point X, and camera centers C and C' are coplanar. This plane is called the epipolar plane and can be determined by the ray back-projecting from x to X and the base line joining the camera centers. The points e and e' where the base line of the cameras intersects with the image planes are called epipoles. Epipoles are actually the images of the camera centers and all epipolar lines must pass through them. In the context of stereo matching algorithms for depth estimation, the search for x' that corresponds to x can be constrained to the epipolar line instead of the whole image. Further details of epipolar geometry and its terminology can be found in [17].

C. Fundamental Matrix

The fundamental matrix F is a 3x3 matrix with rank 2 and satisfies the condition that, for any pair of corresponding points x and x' in the two images, the following equality holds:

$$x'TFx = 0 \tag{4}$$

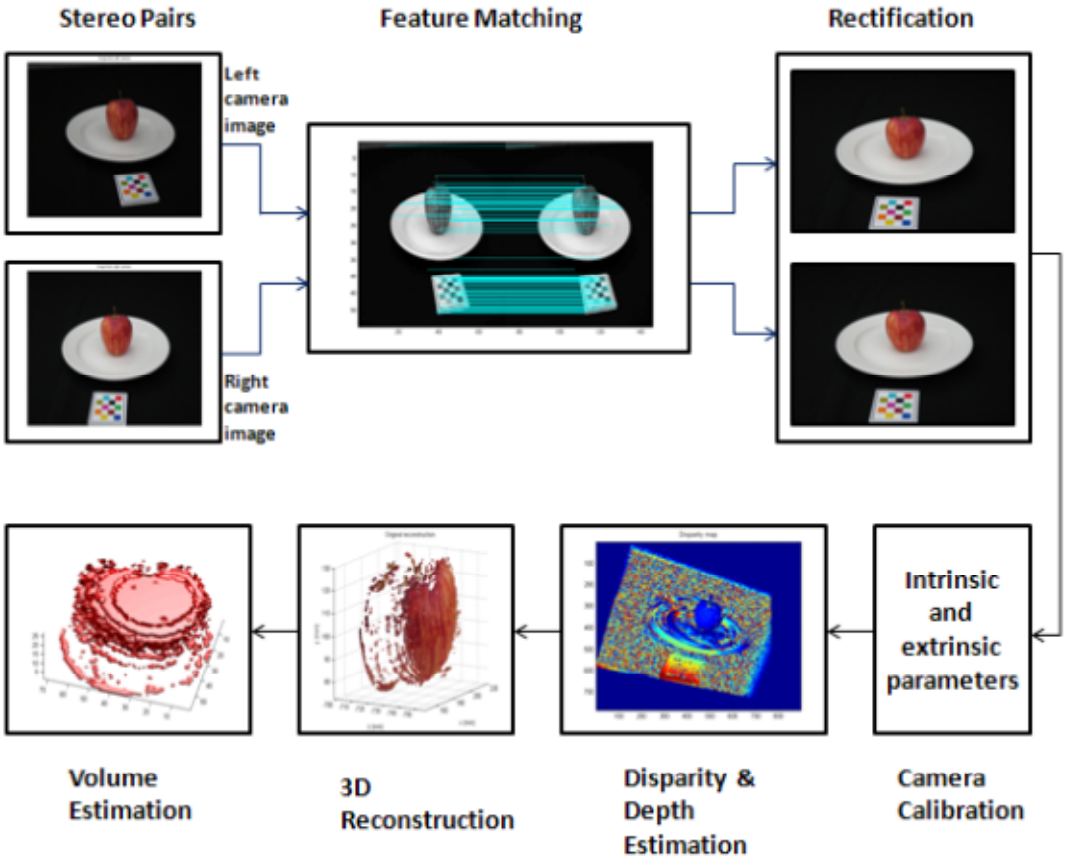

Figure 3. Flow chart of the proposed food estimation approach

According to epipolar geometry, x' lies on the epipolar line $l' = Fx$. Hence $x'^T l' = 0$ and then $x'^T Fx = 0$. We use the strong camera calibration method where the fundamental matrix can be computed using the calibrated camera projection matrices P and P'. Given P and P', the fundamental matrix F can be represented by

$$F = [e]_\times P' P^+ \tag{5}$$

where P^+ is the pseudo-inverse of P, i.e. $PP^+ = I$, and $[a]_\times$ is defined as in (6) when $a = (a_1, a_2, a_3)^T$.

$$[a]_\times = \begin{bmatrix} 0 & -a_3 & a_2 \\ a_3 & 0 & -a_1 \\ -a_2 & a_1 & 0 \end{bmatrix} \tag{6}$$

The fundamental matrix, F can be computed using corresponding points from two views. Given $x = (x,y,1)^T$ and $x' = (x',y',1)^T$, the equation (4) can be rewritten as

$$(x'x, x'y, x', y'x, y'y, y', x, y, 1) f = 0 \tag{7}$$

where $f = (f_{11}, f_{12}, f_{13}, f_{21}, f_{22}, f_{23}, f_{31}, f_{32}, f_{33})^T$ and f_{ij} are the corresponding elements of F. With a set of n point matches, a set of linear equations are obtained as follows

$$Af = \begin{bmatrix} x'_1x_1 & x'_1y_1 & x'_1 & y'_1x_1 & y'_1y_1 & y'_1 & x_1 & y_1 & 1 \\ . & & & & & & & & . \\ . & & & & & & & & . \\ . & & & & & & & & . \\ x'_nx_n & x'_ny_n & x'_n & y'_nx_n & y'_ny_n & y'_n & x_n & y_n & 1 \end{bmatrix} f = 0 \tag{8}$$

F can be computed by solving this set of equations and will be used in the rectification process, which is essential for depth map calculation.

IV. Proposed Food Volume Estimation Approach

Accurate estimation of food portion size from the captured views is one of the challenging problems for the automatic nutritional analysis of food. We have developed a method to automatically estimate the portion size of a variety of foods through volume estimation. Our proposed volume estimation process requires a set of two 2D images to be taken from the left side and the right side of the food items located on the user's plate. The food volume estimation procedure consists of 6 steps: feature matching, rectification, camera calibration, disparity & depth map generation, 3D structure reconstruction and 3D volume estimation. Figure 3 shows a flowchart of the proposed volume estimation approach.

A. Feature Matching

Feature matching identifies the corresponding feature points between the stereo pairs and is used for image rectification. In this paper, we use the SIFT algorithm [19] on the left and right images in order to determine the corresponding feature points. The SIFT algorithm extracts the local features of the objects at particular interest points. The extracted features are not only invariant to image scale and rotation but also robust to changes in illumination, noise, and minor changes in viewpoint. These properties make the extracted features highly distinctive allowing correct object identification with low probability of mismatch. As the rectification process requires at least 8 correct matches, we select the correct matches from the checker board pattern and segmented food region and we remove the rest. An example of the matched points between the stereo images of an apple are shown in Section VI.

B. Stereo Rectification

The fundamental matrix can reduce the search of corresponding points from the whole image to the epipolar line. In practice, a pre-processing procedure known as rectification is usually required in most stereo-matching based disparity and depth estimation algorithms. In our rectification, a pair of images taken from different viewpoints are transformed and re-sampled to produce a pair of rectified images in which the epipolar lines are all parallel with the *x*-axis and are the same in both views. Consequently, the disparity only exists in the *x*-direction. In fact, if the epipolar line is parallel with the *x*-axis after transformation, the epipole will be transferred to the infinite point with the 2D homogeneous image coordinate equal to $(1,0,0)^T$ [17]. Suppose, in the partially transformed left view, a point of interest u_0, i.e. the center of the image, is the origin and the epipole e with a 2D homogenous image coordinate $(f,0,1)^T$ lies on the *x*-axis, then e can be transferred to the infinite point with the following transformation

$$G = \begin{bmatrix} 1 & 0 & 0 \\ 0 & 1 & 0 \\ -1/f & 0 & 1 \end{bmatrix} \tag{9}$$

Finally, the required transformation for rectification of the original left view is given by the product $H = GRT$ where T is the translation taking u_0 to the origin, R is a rotation around the origin taking e to the *x*-axis and G is the transformation which maps e to the infinite point. As for the corresponding rectification transformation H' for the original right view, it can first be computed using a similar method and then optimized by minimizing the sum of squared distance $\sum d(Hx_i, H'x_i')^2$, where x_i and x_i' are corresponding points and $d(x_i, x_j)$ is the distance between the points x_i and x_j . A complete tutorial of image rectification with detailed analysis can be found in [17]. The rectification results for a pair of apple images are shown in the experimental results (Section V).

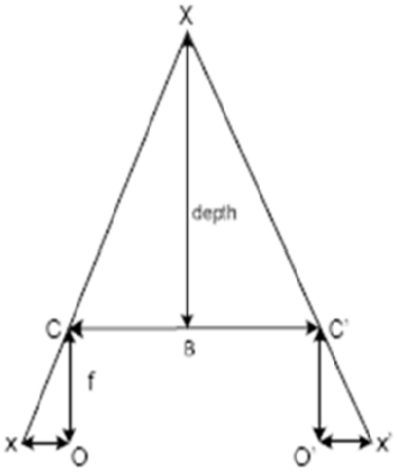

Figure 4. Depth vs. disparity

C. Camera Calibration

Camera calibration is a necessary step in 3D reconstruction to extract metric information from 2D images [18]. In our system, we consider a very simple protocol, which involves the use of a calibrated fiducial marker. It consists of a checker board (color) with known dimensions placed in the field of view of the camera as shown in Figure 3. This allows us to identify the scale and pose of the food item to be estimated and also allows color correction of the images.

The camera parameters consist of intrinsic parameters (focal length, principal point, distortion and skew) and extrinsic parameters (camera orientation and translation). In our food volume estimation process, we use the fiducial marker as a reference to measure the amount of the food present in the plate.

D. Disparity and Depth Map Generation

A disparity map is a depth map where the depth information is derived from offset images of the same scene. Depth maps can be generated using various other methods, such as time-of-flight (sonic, infrared, laser), which we will not explore here. Although these active methods can often produce far more accurate maps at short distances, the passive method has its benefits, including applicability at long distances.

The depth information from the active approaches [20] are either not accurate enough or based on strong assumptions i.e. shape priors or static objects which make them not suitable for multi-view reconstruction applications. In contrast, passive techniques rely solely on images captured by cameras and depth from these approaches (e.g., stereo matching) is straightforward and reliable. The simple principle of depth estimation from stereo matching is illustrated in Figure 4, where B is the length of the baseline joining the camera centers, f is the camera focal length and $disparity = |x - x'|$. Then

$$depth = \frac{Bf}{disparity} \tag{10}$$

which means depth is inversely proportional to disparity and disparity is often treated as synonymous with inverse

depth. The disparity map generated using normalized cross correlation for the apple image is shown in the experimental results (Section VI).

E. 3D Reconstruction

Once the disparity map is estimated, we can convert these disparities into depth using equation (10). With the depth map and knowledge of the intrinsic parameters of the camera, we are able to back project image pixels into 3D points [17, 18]. One way to compute the camera intrinsic parameters is with the MATLAB Camera Calibration Toolbox [21] from the California Institute of Technology. Such a tool will produce an intrinsics matrix, KK, of the form:

$$KK = \begin{bmatrix} fc(1) & alpha\_c * kc(1) & cc(1) \\ 0 & fc(2) & cc(2) \\ 0 & 0 & 0 \end{bmatrix} \quad (11)$$

where fc is a 2×1 vector which contains the focal length in pixels, cc is a 2×1 vector which stores the principal point coordinate, $alpha\_c$ is the skew coefficient (the angle between the x and y axis) and kc is a 5×1 vector, represents the image distortion coefficients.

This camera matrix relates 3D world coordinates to homogenized camera coordinates via

$$\begin{bmatrix} X_{camera} & Y_{camera} & 1 \end{bmatrix}^T = KK \begin{bmatrix} X_{world} & Y_{world} & Z_{world} \end{bmatrix}^T \quad (12)$$

If we know the intrinsic matrix, we can back project each image pixel into a 3D ray that describes all the world points that could have been projected onto that pixel on the image plane. However, the distance of that point to the camera is unknown. This can be recovered by the disparity measurements of the stereo depth map as

$$Z_{world} = focal\_length * \frac{stereo\_baseline}{disparity} \quad (13)$$

Here the pixel disparities are unitless; hence they cannot be used directly in this equation. Also, if the stereo baseline (the distance between the two cameras) is not well-known, then it introduces more unknowns. Thus we transform this equation into the general form

$$Z_{world} = p + \frac{q}{disparity} \quad (14)$$

There are two unknowns in this equation, thus we solve using least squares by collecting a few corresponding depth and disparity values from the fiducial marker and using them as tie points.

In our reconstructed 3D scene, we see only the front view is reconstructed leaving the other part unconstructed. The reason for this is the back view was occluded and we cannot recover the occluded scene thus we use a symmetric reconstruction approach to recover the occluded regions. Symmetry is a universal concept in nature, science, and art. In the physical world, geometric symmetries and structural regularity occur at all scales, from crystal lattices and carbon nano-structures to the human body, architectural artifacts, and the formation of galaxies [22]. Naturally many food objects are symmetric in the real world e.g. apple, orange, pineapple etc. If we can reconstruct half of the food object, we can often easily reconstruct the other half using symmetry.

F. Volume Estimation

In the previous step, the 3D structure of the food item is reconstructed as a 3D point cloud (a set of vertices in a three-dimensional coordinate system). Although point clouds can be viewed and inspected directly, they are not generally directly usable in most 3D applications, and therefore are usually converted to polygons or triangular mesh models, NURBS surface models, or CAD models through a process commonly referred to as surface reconstruction [23].

In our system, we convert the reconstructed 3D point cloud into a series of slices. We accomplish this by dividing the point cloud into several slices. These slices contain exactly the same information as the initial point cloud - the (x,y,z) coordinates of the points. The points of each slice are co-planar, and so we can process each slice as a 2D set of points, instead of a 3D object. The new slices in the 3D body help to access the local information of a particular slice and the information between adjacent slices efficiently, allowing the reconstruction of global structure and the shape of the food object.

We divide the point cloud along the z-axis, which represents the depth information. In our setting, the distance between pixels in the x-axis and y-axis is 1mm and between two slices is also 1 mm. We convert each slice into binary data. The volume estimation process can be performed in two steps: Firstly, the formation of the 2D slices from the 3D point cloud. Secondly, the total volume (V_T) of the food object is the summation of the individual volume (V_k) for each slice which obtained from the previous step. If S is the total number of slices, then we can compute the total volume as follows

$$V_T = \sum_{k=1}^{S} V_k \quad (15)$$

V. Experimental Results

To test accuracy of the proposed food volume estimation approach, we performed validation experiments on 6 fruit items namely: apple, orange, pear, banana, pineapple and kiwi-fruit a shown in Figure 5. A pair (left and right) of images for each category of fruit was captured using an IPhone 4S. The step by step results of the proposed approach are shown in Figure 6 for the apple food item. Table I shows the estimated volume of each food item using or proposed approach and the ground truth volume of the food found using water displacement. The average percentage error for our proposed approach is on average 7.75 % for these food items which is comparable with the accuracy of other more complex approaches.

Our experiments show that the less textured food items may lead to erroneous 3D volume estimation, which can be improved by using an algorithm having better dense matching. Non-uniform lighting condition also can lead to larger errors in the volume estimates.

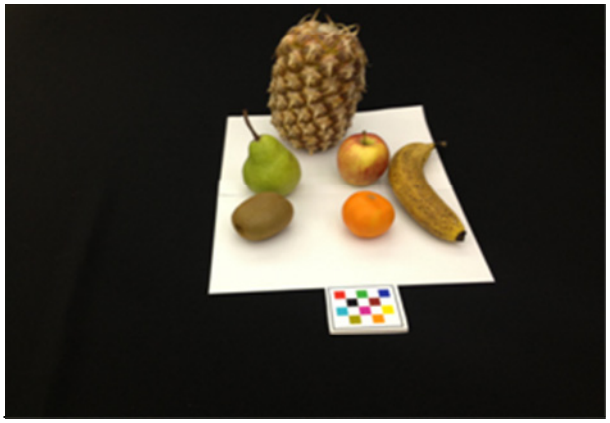

Figure 5. Food items used in our experiments

TABLE I. VOLUME ESTIMATION ERROR (%)

Food Item	Ground truth (ml)	Estimated (ml)	Error (%)
Apple	185	181.5	2.7
Orange	118	112.6	4.6
Pear	230	195.1	15.1
Banana	155	146.5	5.4
Pineapple	1547	1404.2	9.4
Kiwifruit	120	108.8	9.3
Average Error			7.75

VI. CONCLUSIONS AND FUTURE WORK

In this paper, we have proposed a food volume estimation approach by geometrically reconstructing the objects from a pair of stereo images. We consider a free hand approach where the user can capture pictures with minimal restrictions on the position and distance between the cameras. Our image acquisition step requires the inclusion of a fiducial marker in each food image. We obtained the camera parameters and back projected the image plane into 3D world coordinates. We performed experiments for 6 different kinds of popular fruits and estimated their respective volume. Our experimental results show that the proposed approach can provide an accurate estimate of the volume of typical food items in a passive manner without the need for manual fitting of 3D models to the food items.

In future work, we intend to use a 3D stereoscopic camera to obtain the 3D structure and the volume of the food which will eliminate the need for the user to capture two images of the food item and for the complicated rectification process.

REFERENCES

[1] World Health Organization, World Health Assembly resolution WHA57.17 – "Global strategy on diet, physical activity and health." 2003, World Health Organization: Geneva.

[2] World Health Organization, WHO Technical Report Series 916 – "Diet, nutrition and the prevention of chronic diseases," R.o.a.J.W.F.E. Consultation, Editor. 2003: Geneva.

[3] B. M. Margetts, and M. Nelson, "Overview of the principles of nutritional epidemiology," in Design concepts in nutritional

(a) Stereo pair

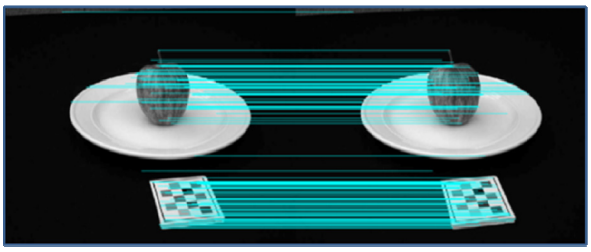

(b) Feature matching

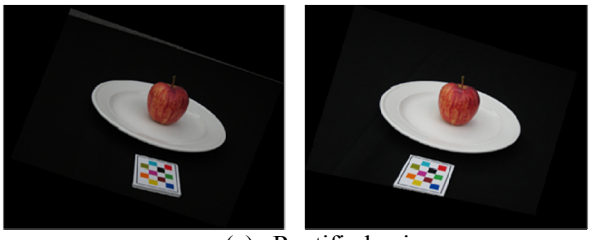

(c) Rectified pair

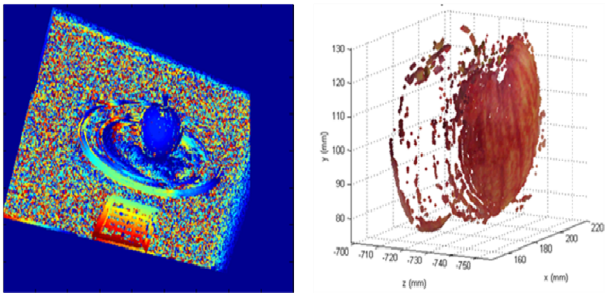

i. Disparity map ii. 3D reconstruction

(d)

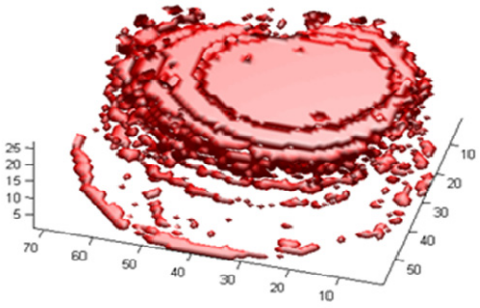

(e) 3D slices (A series of 2D slices)

Figure 6. The step-by-step results of the proposed approach for the apple images.

epidemiology, B.M. Margetts and M. Nelson, Editors. 1997, Oxford University Press: Oxford ; New York. p. 3-38.

[4] Australian Bureau of Statistics, “Cafes, Restaurants and Catering Services, Australia, 2006-07.” 2008, Australian Bureau of Statistics, Canberra.

[5] Australian Government Department of Agriculture Fisheries and Forestry, “FOODmap. A comparative analysis of Australian food distribution channels,” Commonwealth of Australia, Editor. 2006.

[6] J. Dixon, et al., “The health equity dimensions of urban food systems,” J Urban Health, 2007. 84(3 Suppl): p. i118-29.

[7] C. Burns, et al., “Foods prepared outside the home: association with selected nutrients and body mass index in adult Australians,” Public Health Nutr, 2002. 5(3): p. 441-8.

[8] C. J. Boushey, et al., “Use of technology in children's dietary assessment,” European Journal of Clinical Nutrition, 2009. 63: p. S50-S57.

[9] J. T. Tufano and B.T. Karras, “Mobile eHealth interventions for obesity: a timely opportunity to leverage convergence trends,” J Med Internet Res, 2005. 7(5): p. e58.

[10] J. Shang, et al., "A pervasive Dietary Data Recording System," Pervasive Computing and Communications Workshops (PERCOM Workshops), 2011 IEEE International Conference on , pp. 307-309, 21-25 March 2011.

[11] J. Shang, et al., “Dietary intake assessment using integrated sensors and software.” Proc. SPIE 8304, Multimedia on Mobile Devices and Multimedia Content Access: Algorithms and Systems VI, 830403, 9 February 2012.

[12] Martin, C.K.; Kaya, S.; Gunturk, B.K.; , "Quantification of food intake using food image analysis," Engineering in Medicine and Biology Society, 2009. EMBC 2009. Annual International Conference of the IEEE , pp.6869-6872, 3-6 Sept. 2009.

[13] Weiss, R., Stumbo, P.J., Divakaran, A., “Automatic Food Documentation and Volume Computation Using Digital Imaging and Electronic Transmission,” Journal of the American Dietetic Association, Volume 110, Issue 1, January 2010, Pages 42-44.

[14] Chen, H.-C., et al., "3D/2D model-to-image registration for quantitative dietary assessment," Bioengineering Conference (NEBEC), 2012 38th Annual Northeast , pp.95-96, 16-18 March 2012.

[15] Woo I., et al., “Automatic portion estimation and visual refinement in mobile dietary assessment,” Proc. SPIE 7533, Computational Imaging VIII, 75330O, January 27, 2010.

[16] Chae, J., et al., “Volume estimation using food specific shape templates in mobile image-based dietary assessment.” Proc. SPIE 7873, Computational Imaging IX, 78730K, February 07, 2011.

[17] R. Hartley and A. Zisserman, “Multiple View Geometry in Computer Vision”, Second Edition, Cambridge University Press, UK, 2003

[18] Zhang, Z., "A flexible new technique for camera calibration," Pattern Analysis and Machine Intelligence, IEEE Transactions on, vol.22, no.11, pp. 1330- 1334, Nov 2000

[19] David G. Lowe, “Distinctive Image Features from Scale-Invariant Keypoints”, Int. J. Comput. Vision,60(2), 91-110, Int. J. Comput. Vision, 2004

[20] S.B. Gokturk, H. Yalcin, and C. Bamji. “A time-of-flight depth sensor- system description, issues and solutions.” In CVPRW, 8, 24, page 35, june 2004.

[21] http://www.vision.caltech.edu/bouguetj/calib_doc/htmls/parameters.html

[22] N. J. Mitra and M. Pauly and M. Wand and D. Ceylan, "Symmetry in 3D Geometry: Extraction and Applications”, 33rd Annual Conference of the European Union for Computer Graphics (Eurographics 2012), Cagliari, Italy, May 13-18.

[23] S. Rusinkiewicz and M. Levoy, QSplat: a multiresolution point rendering system for large meshes. In Siggraph 2000. ACM , New York, NY, 343–352.